



Full Length Article

# Influence of alkali metal Na on coal-based soot production

Ziqi Zhao, Qian Du<sup>\*</sup>, Dun Li, Heming Dong, Jianmin Gao, Haibo Li, Yu Zhang

*Institute of Combustion Engineering, School of Energy Science and Engineering, Harbin Institute of Technology, Harbin, Heilongjiang 150001, PR China*



## ARTICLE INFO

## Keywords:

Soot  
Na  
Pyrolysis  
Oxidation  
Catalytic mechanism

## ABSTRACT

This work aims to investigate the effects of Na on the characteristics of coal-derived soot. Soot, which has long been regarded as an unwelcome source of air pollution, has been classified as a pollutant. However, with the proposed clean and efficient utilization of coal, soot has been found to be effectively inhibited by adding metal catalysts and changing the reaction environment, and it can even realize the transformation of pollutants to functional materials. To understand the effect on physiochemical properties, pyrene was used as a coal tar substitute, and the structural transformation of soot was thoroughly investigated by DFT calculation method in combination with elemental analysis, transmission electron microscopy, X-ray diffraction, Raman spectroscopy, Fourier transform infrared spectroscopy, and X-ray photoelectron spectroscopy. The presence of Na changed the  $\pi$  electron distribution of benzene ring, promoted the dehydrogenation condensation and oxidation exfoliation of the surface microchip layer, and accelerated the condensation of PAHs and the formation of five-membered ring in the microchip layer. Na participates in the oxidation and growth process of soot, which can regulate the micromorphology of soot. With the participation of Na, the diameter of soot particles decreases, the microcrystal length and curvature become larger, and the internal holes increase.

## 1. Introduction

Energy is the cornerstone of national development, and the energy issue is the fundamental problem of human social development. Coal consumption account for 27.2% of the global energy consumption in 2020; coal is highly prone to producing pollutants and waste throughout the utilization process compared with oil, natural gas, and other fossil energy [1,2]. Carbon emissions from coal production and consumption account for 70%–80% of the total domestic carbon emissions. Many researchers have conducted research on clean and renewable fuels under the context of “carbon peak” and “carbon neutrality”. For example, microorganisms, animal fat, and waste oil are used to produce biodiesel [3,4], electrolysis of CO<sub>2</sub>/H<sub>2</sub>O into sustainable hydrocarbon fuel [5,6], and electrolysis of hydroxide and water to produce hydrogen [7,8], and biomass renewable fuel [9]. However, the world still needs coal due to the imperfect development and high cost of new renewable and clean energy at the present stage. The coal industry will not go away, but it will undergo transition and transformation to clean coal [10]. Coal classification, transformation and utilization are among the effective methods for addressing the environmental pollution and resource waste generated through coal processing.

Coal tar is a by-product of coal grading conversion and utilization

and an important chemical raw material with a complex composition and abundant polycyclic aromatic hydrocarbons (PAHs), such as naphthalene, pyrene, and heterocyclic compounds containing oxygen, sulfur, and nitrogen [11]. These PAHs, as the precursors of soot, can form soot through pyrolysis or anoxic combustion. Soot particles with a large specific surface area and a small particle size (<2.5  $\mu\text{m}$ ) are ubiquitous in the atmosphere. These particles also cause air pollution and global warming [12]. Moreover, soot particles are deposited in alveolar cells into the blood circulation system, causing respiratory diseases, cardiovascular diseases, and even cancer, inflicting significant harm to the human body [13–16]. Soot has long been used as a contaminant in prevention and control. Many researchers have discovered that high-quality soot is a good chemical material that can be classified into “reinforcing carbon black”, “conductive carbon black”, and “wear-resistant carbon black” based on the carbon black performance [17,18]. Therefore, the growth and oxidation mechanism of soot must be studied from the theoretical and practical perspectives for the transition from “pollutant soot” to “functional carbon black” [19–21].

Many academics have recently studied soot produced by hydrocarbon fuels, diesel emission soot, candle combustion [22,23], and biomass pyrolysis. The results showed that soot can control the reaction temperature, residence time, and reaction atmosphere, add metal catalyst

<sup>\*</sup> Corresponding author.

E-mail address: [duqian@hit.edu.cn](mailto:duqian@hit.edu.cn) (Q. Du).

<https://doi.org/10.1016/j.fuel.2022.124327>

Received 14 March 2022; Received in revised form 19 April 2022; Accepted 21 April 2022

Available online 20 May 2022

0016-2361/© 2022 Elsevier Ltd. All rights reserved.

[24], and realize the directional regulation of soot, thereby reducing emissions or even resource utilization. However, this research focuses on the catalytic oxidation of alkali metal on soot. Mannazhi and Simonsson et al. [25,26] proved that metal K can enhance the ionization of initial soot particle via two methods, namely, 2D laser-induced incandescence and laser-induced fluorescence, resulting in increased electrostatic potential repulsion between soot precursors and suppressing the coalescence and growth of soot. Although there are certain controversies regarding the effect of Na on soot generation, and some studies [27–29] found that Na mainly inhibits soot generation, doping sodium will promote the oxidation rate of soot particles, while Na may inhibit soot nucleation through charge transfer. Other studies [30] found that a low concentration of Na gasification increased soot yield by promoting the aggregation of aromatics and forming a disordered core of soot. Li et al. [31] obtained an anode material for sodium ion batteries by one-step carbonization of pyrolysis anthracite, which exhibited an excellent reversible specific capacity and a good cycling stability. At present, some results have been achieved in the simulation of PAH oxidation reaction. Edwards et al. [32] calculated the oxidation pathway of  $\bullet\text{OH}$  on phenanthrene radicals by density flooding theory and found that the reaction is mainly controlled by the migration or removal of H atoms from  $\bullet\text{OH}$  and the subsequent release of CO from the radical decomposition. Frenklach et al. [33] studied the oxidation of aromatic hydrocarbon radicals by  $\text{O}_2$ ,  $\bullet\text{OH}$  and O and confirmed the H migration phenomenon in the  $\bullet\text{OH}$  oxidation reaction. However, there is a lack of theoretical support for the influence of alkali metals on the soot generation process. The above-mentioned studies have shown that Na can influence the formation of coal-based soot and achieve soot resourcefulness. However, the effects of Na on coal-based soot generation remain largely unclear due to the nature of soot generation and the complexity of coal composition.

In this study, pyrene, a typical component of coal tar, was selected as the reactant. The influence of alkali metal Na on soot generation was explored via experiments and simulation. This mechanism is a promising way to develop and adjust the structural characteristics. Turn soot from a pollutant to a functional material that can be used for energy storage, particularly for sodium ion battery development.

## 2. Methodology

### 2.1. Coal samples

Molded coal powder was created in this study by loading molded components onto synthetic coke particles that were almost completely carbon. The synthetic coke is composed of nanoscale carbon powder as aggregate and sucrose as binder. The temperature is increased to 500 °C at a rate of 1 °C/min in a muffle furnace under  $\text{N}_2$  atmosphere and held for 30 min. After the volatile matter is removed, the particle size was obtained by sieving the particles between 38  $\mu\text{m}$  and 125  $\mu\text{m}$ . The loading process was carried out by dissolving the model compound and synthetic coke in anhydrous ethanol in the ratio of 3:7. Then, the deionized water solution of  $\text{NaNO}_3$  was added according to the mass ratio of Na in the final molded coal powder of 0% and 1%. Subsequently, the ethanol and water were evaporated by heating in a water bath after vigorously stirring. Finally, the molded coal powder was dried and ground, and pulverized coal particles with particle sizes ranging from 38  $\mu\text{m}$  to 125  $\mu\text{m}$  were taken for experiments.

The Na content of the molded coal powder was measured via inductively coupled plasma optical (ICP-OES) emission spectrometry

before the trials. The results (Table 1) showed that the Na content in the molded coal powder increased from 0.09 wt.% to 0.82 wt.% before and after  $\text{NaNO}_3$  loading, with a strong loading effect.

### 2.2. Pyrolysis apparatus

Fig. 1 depicts the experimental pyrolysis [9] system. A high-temperature sinker furnace with an 80 mm diameter and 1000 mm height corundum tube in the center is at the heart of the system. Six silicon molybdenum rods are positioned between the outer polycrystalline fiber liner and the corundum tube to heat the furnace chamber. The furnace chamber temperature is measured and controlled with a platinum–rhodium S-type thermocouple on the exterior wall of the corundum tube in the middle of each segment. The experimental temperatures were all maintained at 1250 °C.

### 2.3. Characterization method

The characterization of soot was mainly divided into three parts: elemental ratio, microstructure, and chemical structure. During the elemental analyses, the elemental contents of C, H, and N in soot were measured with a CHN elemental analyzer. The C1s and O1s high-resolution spectra were measured with a monochrome Al-K Alpha gun in the measuring point range of 500 m on the sample surface to obtain C/O elemental ratios [34].

The microstructure of soot was cross-characterized by scanning electron microscope (SEM, Regulus8100), transmission electron microscopy (TEM, JEM-2100F), Raman spectra (Raman, Horiba Jobin-Yvon LabRAM HR800), and X-ray diffraction (XRD, D/max-2550VB/PC, RIGAKU). SEM was used for the three-dimensional structure and surface morphology of soot [35,36]. TEM was performed to observe the microstructure and particle size distribution of soot [37]. Approximately 1 mg of soot was dissolved in 1.5 ml of absolute ethanol and sonicated for 30 min. The suspension droplets were then dried on a TEM grid and analyzed by digital microimage software. The Raman spectra of soot samples were obtained using a laser wavelength of 532.15 nm and a 50 $\times$  objective optical microscope, and at least 5 lines were measured for each sample, with each exposure time of 12 s [38]. The XRD of soot was recorded using a Cu radiation source ( $\lambda = 0.154056$  nm) to collect signals from soot samples in the range of  $2\theta = 10^\circ\text{--}80^\circ$  [39].

The functional groups of the soot samples were characterized by Fourier transform infrared spectroscopy (FTIR, Nicolet 5700) and X-ray photoelectron spectroscopy (XPS). The samples were scanned 32 times with an FTIR spectrometer to obtain the FTIR spectra with a spectral range of 400  $\text{cm}^{-1}$  to 4000  $\text{cm}^{-1}$  and a resolution of 4  $\text{cm}^{-1}$  [40]. At least two FTIR spectra were measured per sample. The final spectrum was the addition of two FTIR spectra with high similarity to ensure the reliability of the samples.

### 2.4. Computational details

#### 2.4.1. Electronic structure calculations

All calculations were performed using density functional theory (DFT) with the M06-2X functionals in Gaussian 09. The 6-31G(d) basis set was used to characterize the atoms. The molecular model construction was performed in GaussView, a graphical user interface program developed specifically for Gaussian users to create input files and view output results. Wave function analysis was performed in Multiwfn [41] program, which is an analysis program based on the wave function information produced by the quantum chemical program. Previous research [42,43] has shown that M06-2X/6-31G(d) can improve the calculation accuracy and reduce the computation time. In this study, the geometry of the reactant, intermediate, product, and single point energy were obtained at the M06-2X/6-31G(d) level. Intrinsic reaction coordinate calculations were performed in combination with the D3 method for the correction of dispersion to verify the transition state structures

**Table 1**  
Na content in the two samples.

Synthetic coal	Na (wt. %)
Pye	0.09
Pye-Na	0.82

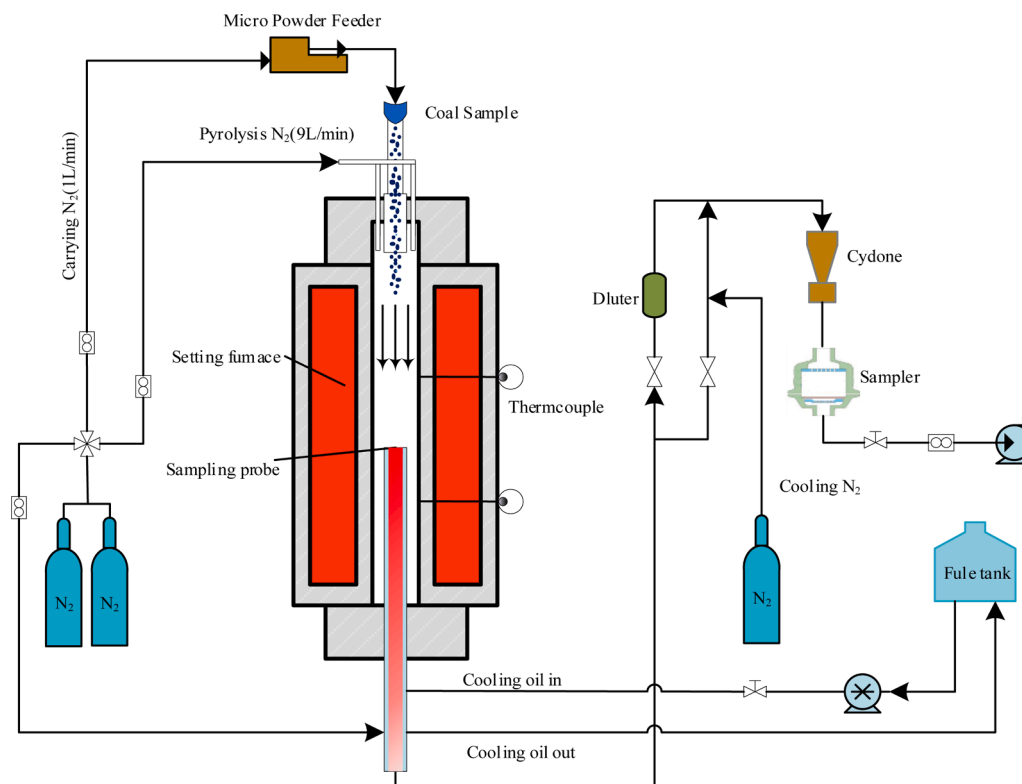


Fig. 1. Schematic of the experimental system.

[44]. In the calculation process, the strength of chemical bonds in molecules was calculated using the Laplacian bond order (LBO) [45] and bond length. The larger the bond order, the shorter the length of the

chemical bond.

In comparison with closed aromatic rings, free radicals are more likely to react with other molecules between them. This work proves this

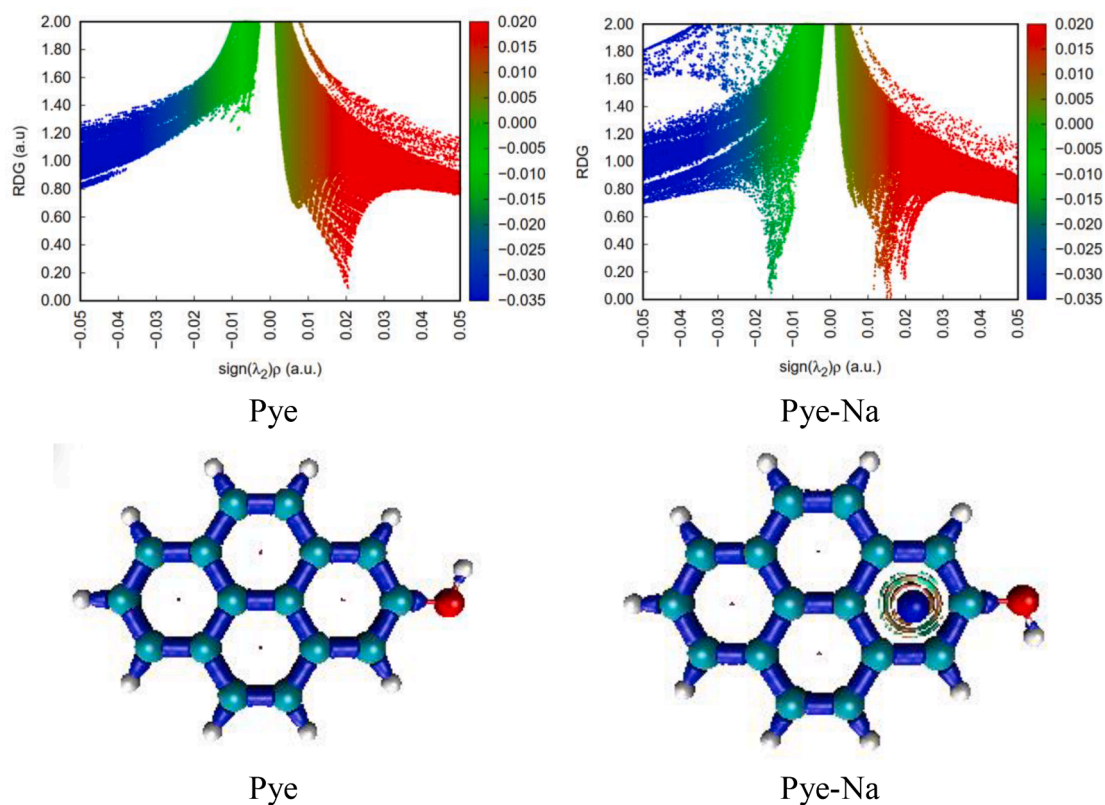


Fig. 2. The scatter plots and IRI iso-surface plots of Pye and Pye-Na.

notion by comparing the binding energy of benzene ring and benzene radical with  $\cdot\text{OH}$ . The binding energy of benzene ring with hydroxyl radical is  $-18.60$  kcal/mol, which is much lower than that of phenyl with a hydroxyl radical of  $-114.56$  kcal/mol, indicating that the radical can easily bind with  $\cdot\text{OH}$ . Therefore, the chemical reaction of pyrene radical with  $\cdot\text{OH}$  was chosen to verify the effect of alkali metal Na on the oxidation of PAHs.

#### 2.4.2. Intermolecular forces

In the early stages of the chemical reaction, the molecules first approach each other by electrostatic attraction, which is a process that depends on the electrostatic effect of the molecule on its surrounding environment. Yang et al. [46] proposed and visualized noncovalent interactions (NCI) based on a reduced density gradient (RDG) to facilitate the study of weak molecular interactions. Which uses density and its derivatives that allow simultaneous analysis and visualization of a wide range of noncovalent interaction types as realistic spatial surfaces is currently an important tool for performing chemical analysis.

Multiwfn [47] presents the scatter diagram and the interaction region indicator (IRI) [44] iso-surface diagram of "Pye" and "Pye-Na" (Fig. 2). The IRI iso-surface diagram depicts the red spindle areas in the middle of the benzene rings, which corresponds to the spike at the far right of the scatter plot, reflecting a strong position resistance effect. The IRI surface between the benzene ring and the sodium atom is partly orange and partly green, corresponding to the spike tip  $\times$  values of approximately  $+0.016$  and  $-0.017$  on the scatter plot.

### 3. Results and discussion

#### 3.1. Surface oxidation reaction

Hydrogen atom transfer and oxygen radical decomposition are the two main processes in the oxidation of PAHs radicals by  $\cdot\text{OH}$ . The  $\cdot\text{OH}$  oxidation of pyrene radicals is separated into two reaction pathways (Fig. 3), depending on the binding site of  $\cdot\text{OH}$  in the pyrene molecule [48,49]. Both processes begin with hydrogen atoms in  $\cdot\text{OH}$  being transferred to nearby carbon atoms. The migration of hydrogen atoms allows the rapid rearrangement of the bound  $\cdot\text{OH}$  aromatic ring to form kinetically favorable oxygen radicals for decomposition, facilitating the breakage of the C–C bond in the benzene ring.

The oxidation of pyrene radical by  $\cdot\text{OH}$  starts with H-atom transfer,

as shown in Fig. 3. In Path 1, R1 forms the intermediate A1 by hydrogen atomic transfer, with the required energy exceeding 73.24 kcal/mol, which is the speed control step for the entire reaction. Fig. 4 shows the bond length and LBO of each C–C in A1, where the C11–C12 bond is longer, and the LBO is smaller, which is a weak bond in the system and prone to breakage. In  $\text{TS}_{\text{A1-I1}}$ , the bond elongates to 2.166 Å. The bond angles of C9–C11–C12 and C11–C12–C13 dilate to  $104.34^\circ$  and  $103.17^\circ$ , respectively. The aromatic ring significantly deforms and finally completely breaks to form the stable intermediate I3. C9 and C12 then bond through  $\text{TS}_{\text{I1-J1}}$  to form J1 containing a five-membered ring. In the final step of the reaction,  $\text{TS}_{\text{J2-P}}$ , the bond between C11 and C9 is elongated to 1.468 Å and finally breaks to form P and release CO. The plausibility of this process was also confirmed by Frenklach et al. [50] in their simulation of the formation of soot in a flame environment by KMC.

The bond lengths and LBO calculations for the intermediate A2 formed by the H migration of R2 in Path 2 are shown in Fig. 4(c) and 4(d). C11–C12 is a weak bond in the system. The bond elongates to 2.239 Å in transition state  $\text{TS}_{\text{I2-P}}$  (bond angles of  $106.87^\circ$  and  $99.97^\circ$  for C9–C11–C12 and C11–C12–C13, respectively) and eventually breaks to form intermediate I2, which also results in the formation of P and the release of CO.

According to the energy barrier diagram [51], the rapid control steps of both pathways are H-transfer processes, and the reaction energy barrier that Path2 needs to overcome is 71.23 kcal/mol which is lower compared with 73.24 kcal/mol of Path1. The energy barrier of Path2 in the third reaction step is 44.04 kcal/mol which is much lower than 64.15 kcal/mol of Path1. Therefore, the reaction of  $\cdot\text{OH}$  oxidation of pyrene radical tends to follow Path2 more.

According to the electron transfer mechanism,  $\text{Na}^+-\pi$  bonds are formed between sodium and pyrene radicals, and sodium acts as an electron acceptor to change the  $\pi$  distribution of the benzene ring, making it easier for the pyrene radicals to bond with  $\cdot\text{OH}$ . The reaction paths and reaction energy barriers involved in the  $\text{Na}^+-\pi$  structure are shown in Fig. 5. The  $\cdot\text{OH}$  binding position is the same as Path2 in Fig. 3.

Given that the attraction of  $\text{Na}^+$  to O in the  $\text{Na}^+-\pi$  structure promotes O–H breaking, the first step of the reaction in Fig. 5 is also H migration. Meanwhile, in the transition state  $\text{TS}_{\text{R2-A2}}$ , Na and O are attracted to each other and form a stable chemical bond in intermediate A2. The calculation of the bond length and LBO of A2 shows that the C–C bond length (1.517 Å) is the largest and the bond level (1.068) is the lowest

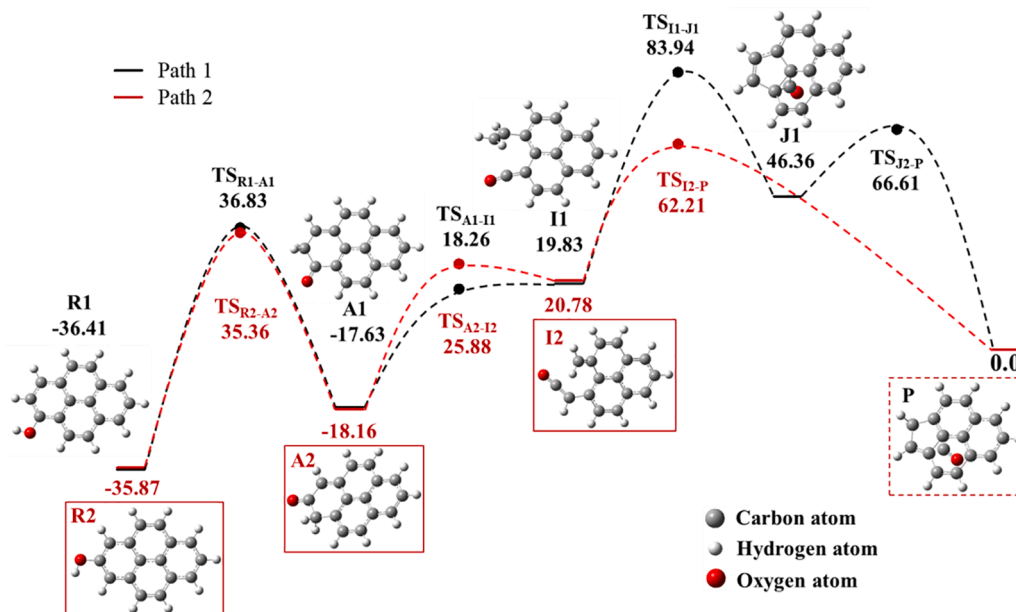


Fig. 3. Two reaction pathway and energy diagram of  $\cdot\text{OH}$  oxidizing pyrene radical.

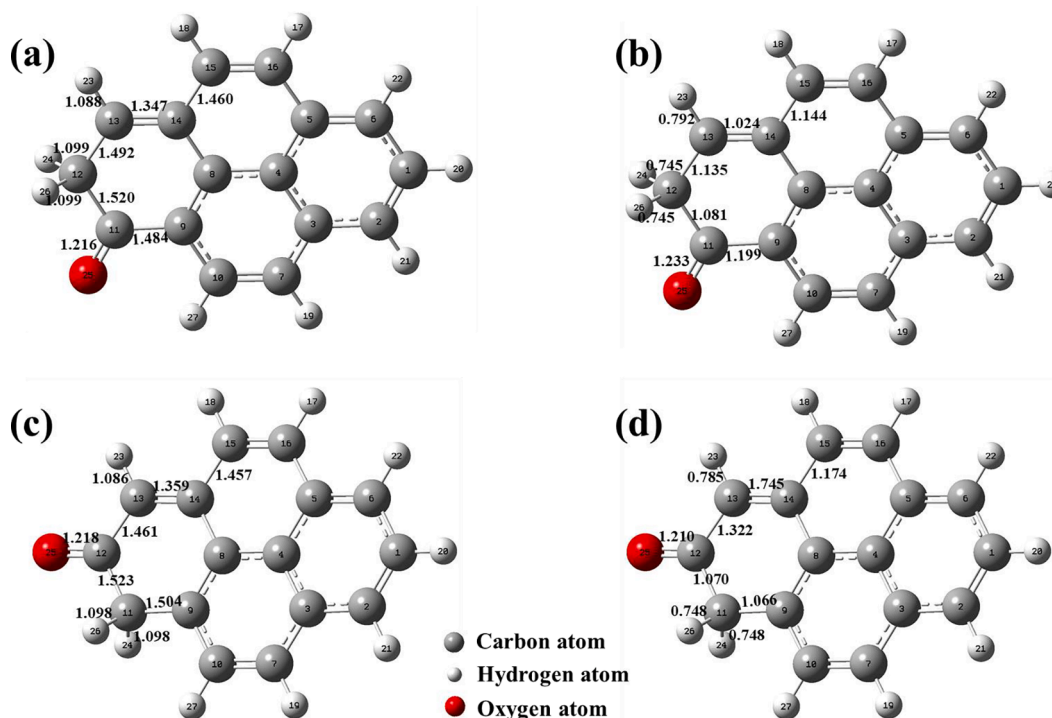


Fig. 4. Bond length (left, unit: Å) and LBO (right) of the intermediate P1-A1 and P2-A2.

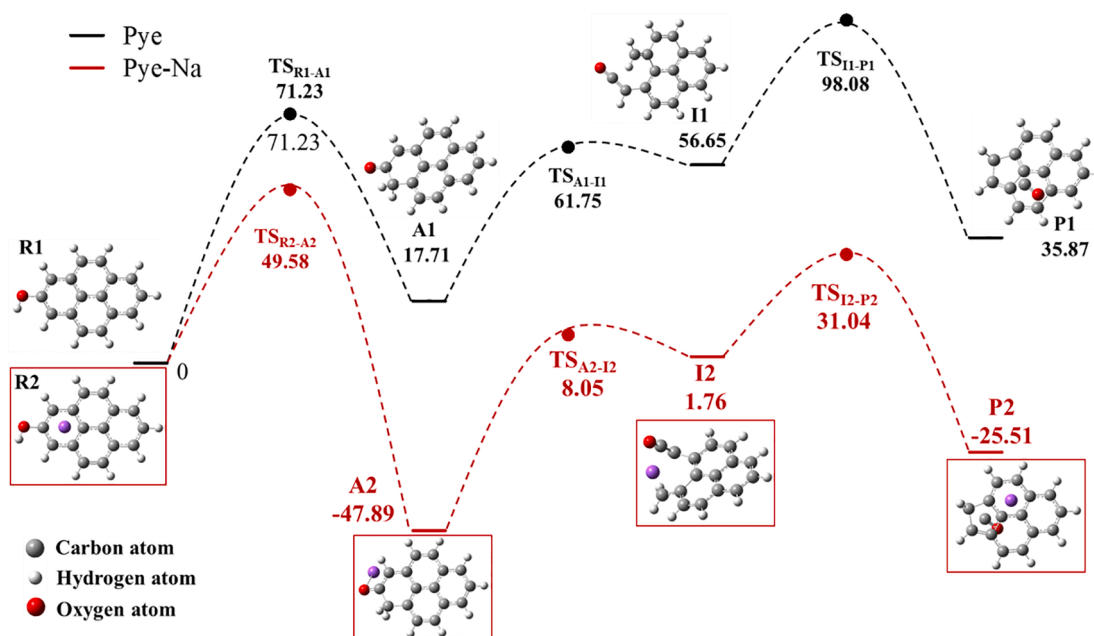


Fig. 5. The reaction path and energy diagram of  $\text{Na}^+$  catalyzed the oxidation of pyrene radical by  $\cdot\text{OH}$ .

between the carbon atom bound by the oxygen-containing structure and the carbon atom receiving the migrating H. Accordingly, the bond length increases to 2.533 Å in the second step of reaction transition state A2  $\rightarrow$  I2 and finally breaks in intermediate I2. The Na–O bond is also broken in the second step of the reaction, releasing the free  $\text{Na}^+$ . The broken six-membered ring then forms a five-membered ring again and releases CO, and Na + is complexed with the aromatic ring through the  $\text{Na}^+\text{-}\pi$  structure. The reaction energy barrier for H migration in the first step of the reaction is 49.58 kcal/mol. Meanwhile, while the reaction energy barrier in the second step of the reaction catalyzed by the  $\text{Na}^+\text{-}\pi$  structure is only 55.94 kcal/mol, both of which are much lower than the

H migration energy barrier without Na addition (71.23 kcal/mol for the rapid control step), demonstrating that the  $\text{Na}^+\text{-}\pi$  structure can promote the oxidation of PAHs by oxygenates and the formation of five-membered rings in the carbon microchip layers [52,53].

### 3.2. Validation and predictions

#### 3.2.1. Element atomic ratio

Table 2 shows the elemental contents of C, H, and N in the soot measured with a CHN elemental analyzer. The atomic ratios of the different elements in the soot samples are shown in the figure, where C/

**Table 2**  
The main element contents in synthesis coals.

Synthetic coal	N (wt. %)	C (wt. %)	H (wt. %)
Pye	0.275	97.495	1.1745
Pye-Na	0.225	97.74	1.052

O is obtained from XPS, and C/H is acquired from CHN. The sources of oxygen in the pyrolysis products are O released from  $\text{NO}_3^-$  and  $\text{O}_2$  adsorbed on the surface of synthetic coke.

The carbon to hydrogen atom ratio (C/H) [54] has been applied in the study of soot characterization for a long time. In the study of coal-derived soot, the higher the soot conversion rate of tar, the higher the graphitization of soot, and the greater the C/H value because the conversion of PAHs into soot involves dehydrogenation and condensation [55–57]. Table 3 illustrates that the contents of C/H and C/O increase after Na addition, indicating that Na may promote the growth and oxidation of soot, but it needs to be analyzed and verified by subsequent testing methods.

### 3.2.2. Soot microstructures

The TEM works by changing the direction according to the collision of electrons projected onto the sample with the atoms in the sample, resulting in stereoscopic angular scattering and formation of different images of light and shadow. We chose the scale of 200 nm to examine the aggregation state of soot particles and 50 nm to observe the microchip layer morphology. Fig. 6 depicts the SEM images of Pye soot and Pye-Na soot, showing the three-dimensional structure of soot particles [35]. From Fig. 6, it can be seen that the pyrene pyrolysis products are uniformly distributed round particles, Na has less influence on the three-dimensional morphology of soot particles, so the internal microstructure of soot particles were characterized by TEM. Fig. 7 presents the typical TEM images of pyrene pyrolysis derived soot particles. Soot consists of primary particles that form fractal aggregates of several hundred nanometers. In this study, the particle size distribution and fractal dimension of basic soot particles of soot aggregates were extracted by ImageJ [58]. The number of extracted particles in the low magnification TEM images of both conditions is more than 200 to ensure the accuracy of the extracted elementary soot particle size data.

Fig. 8 shows that the particle size range before the Na addition is between 15 nm and 45 nm and increases to 55 nm after Na addition. The peak particle size of Pye-Na pyrolysis-derived basic soot is 25–30 nm, which is reduced compared with the 30–35 nm of Pye-soot. This result indicates that the inhibition of the basic soot particle size growth by gasification Na in the pyrolysis gas is obvious. This phenomenon occurs because Na has a low ionization potential and can be strongly ionized in the pyrolysis gas, affecting the agglomeration between basic soot particles through particle charge exchange and, reducing the formation of soot aggregates, and Na can promote pyrolysis. The oxidation of soot by oxygen-containing substances in the gas results in the consumption of the microchip layer on the surface of soot particles, which inhibits the growth of soot particles.

Fig. 9 shows the length and curvature distribution of the graphite-like crystallites in the basic soot particles. The length of the graphite-like crystallites in the basic soot particles is shorter than 2.0 nm, and the average curvature is in the range of 1.1–1.13. The average value of the length and curvature of the graphite-like crystallites increased with the addition of Na. However, given the small difference in the microchip length, a series of nanostructural parameters, including the length of the

**Table 3**  
The C/H and C/O content in Pye and Pye-Na.

	Pye	Pye-Na
C/O	13.45	16.06
C/H	6.92	7.74

graphite-like microchip layers in soot, is obtained by resolving the Raman tests in the later section.

Fig. 10 shows the first-order Raman spectra of the pyrene pyrolysis-derived soot samples before and after the addition of Na. Raman spectroscopy is a technique used to measure the frequency shift between the scattered and then incident photons when incident photons is inelastic with the sample [59–61]. The Raman spectral map is composed of a certain number of Raman peaks, each corresponding to a specific molecular bond vibration. In Fig. 10, Na hardly affects the  $D_1$  peak position ( $1350\text{ cm}^{-1}$ ) and G peak position ( $1580\text{ cm}^{-1}$ ). The D peak indicates the carbon's disordered structure, whereas the G peak denotes the carbon's graphitized structure [62,63]. To better evaluate the microcrystalline structure of soot, it was deconvoluted into five bands according to the method described in Saffaripour [64]. Fig. 10 is a schematic diagram of the peaks of the Raman spectrum of soot. Five peaks in the range of  $800\text{--}2000\text{ cm}^{-1}$  can be observed. The  $D_1$  peak is a graphitic structure defect peak, which is associated with planar defects in the carbon structure (heteroatoms, etc.) and graphitic defects [65,66]. The sharper G peak is related to the  $E_{2g}$  vibrational mode of the defect-free graphite lattice structure.  $D_3$  is related to the presence of amorphous carbon and organic molecules [67]. The  $D_4$  peak is often at the shoulder of the  $D_1$  peak and represents carbon atoms with  $sp^3$  hybridization and intermediate  $sp^2\text{--}sp^3$  hybridization states and C–C in polyacetylene compounds. The ratio of the area intensity of the  $D_1$  peak to the G peak ( $I_{D1}/I_G$ ) is an important parameter to characterize the size of the carbon microcrystal structures [68,69].

The curve fitting results for the Raman first-order spectra yielded four parameters:  $R_2 = I_{D1}/(I_{D1} + I_G + I_{D2})$ ,  $La = 4.35/(I_{D1}/I_G)$ ,  $I_{D3}/I_{D1}$ , and  $FWTH_G$  [70–72]. Many researchers have used  $R_2$  to characterize the degree of organization of carbon materials [73]. The formula for  $La$  is derived from the results of Tuinstra and Koenig [74] and is an approximation of the characteristic size of graphite microcrystals.  $I_{D3}/I_D$  is used to measure the share of amorphous carbon in soot because the  $D_3$  peak is generated due to the presence of amorphous carbon. The soot full width at half maximum of the G peak [75] is often used as an indicator of the degree of graphitization of soot.

Table 4 shows the changes of these parameters before and after the addition of Na. After the addition of Na, the  $R_2$  of pyrene pyrolysis-derived soot decreased, and  $I_{D3}/I_G$  and  $FWTH_G$  increased. This finding indicates that the ordered microcrystalline structure in soot was oxidized after the addition of Na, the organization of the microchip layer was weakened, and the amorphous carbon content increased. Zhang et al. [76]. also found that the addition of Na exhibits a higher promotion on increasing structural defects of carbon in the study of diesel soot.  $La$  increased from 1.54 to 1.74, and the carbon microcrystalline structure gradually grew during the oxidation of soot, which was also confirmed in the study of Ishiguro [77].

Fig. 11 shows the XRD spectrum of the soot particles, where two characteristic peaks in the  $2\theta$  range  $10\text{--}60^\circ$  can be seen in both soot types, which is consistent with the results in [78,79]. The broad band at  $2\theta = 24.5^\circ$  represents the 002 plane, which is a set of graphite-like layers of crystalline planes in the vertical tube diameter direction in the carbon materials. The  $d_{002}$  value is commonly used to characterize the layer spacing between each layer. A narrow band can be observed at about  $2\theta = 44^\circ$ , which represents the 100 plane, which intensity reflects the proportion of ordered carbon structure. Fig. 11 demonstrates no significant change in the peaks before and after the addition of Na. Therefore, the carbon microchip layer spacing  $d_{002}$ , layer height  $Lc_{(0\ 0\ 2)}$ , layer structural size  $La_{(1\ 0\ 0)}$ , and the average layer number  $n$  of the layer structure are introduced to analyze and calculate the carbon microchip structural parameters. The estimation method for the four microcrystalline parameters were described in the literatures [78,80,81].

Table 5 displays that Pye = Pye-Na greater than 0.3554 nm in  $d_{002}$ , and 0.3554 nm is the standard graphite structure. Hence, pyrene pyrolytic soot is a mixture of disordered carbon structure and partially ordered carbon microcrystalline structure, but Na has less effect on this.

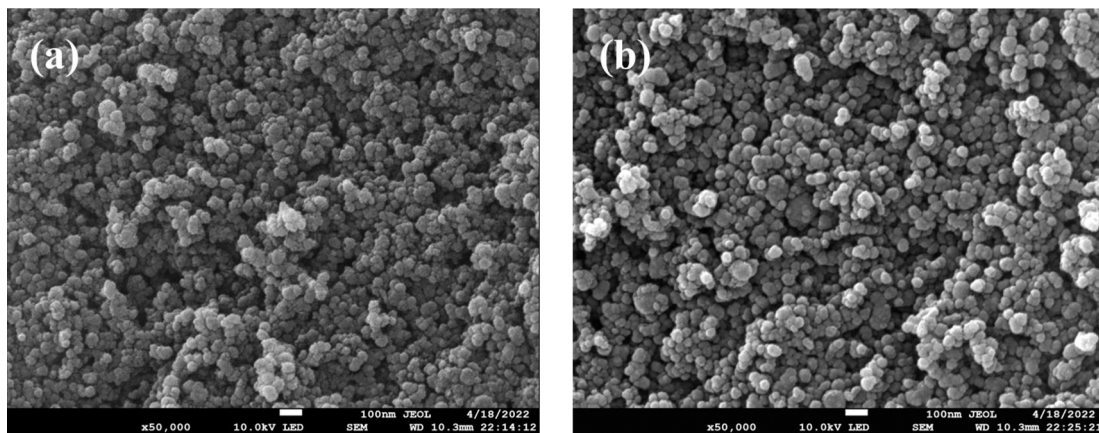


Fig. 6. SEM images of soot (a) Pye; (b) Pye-Na.

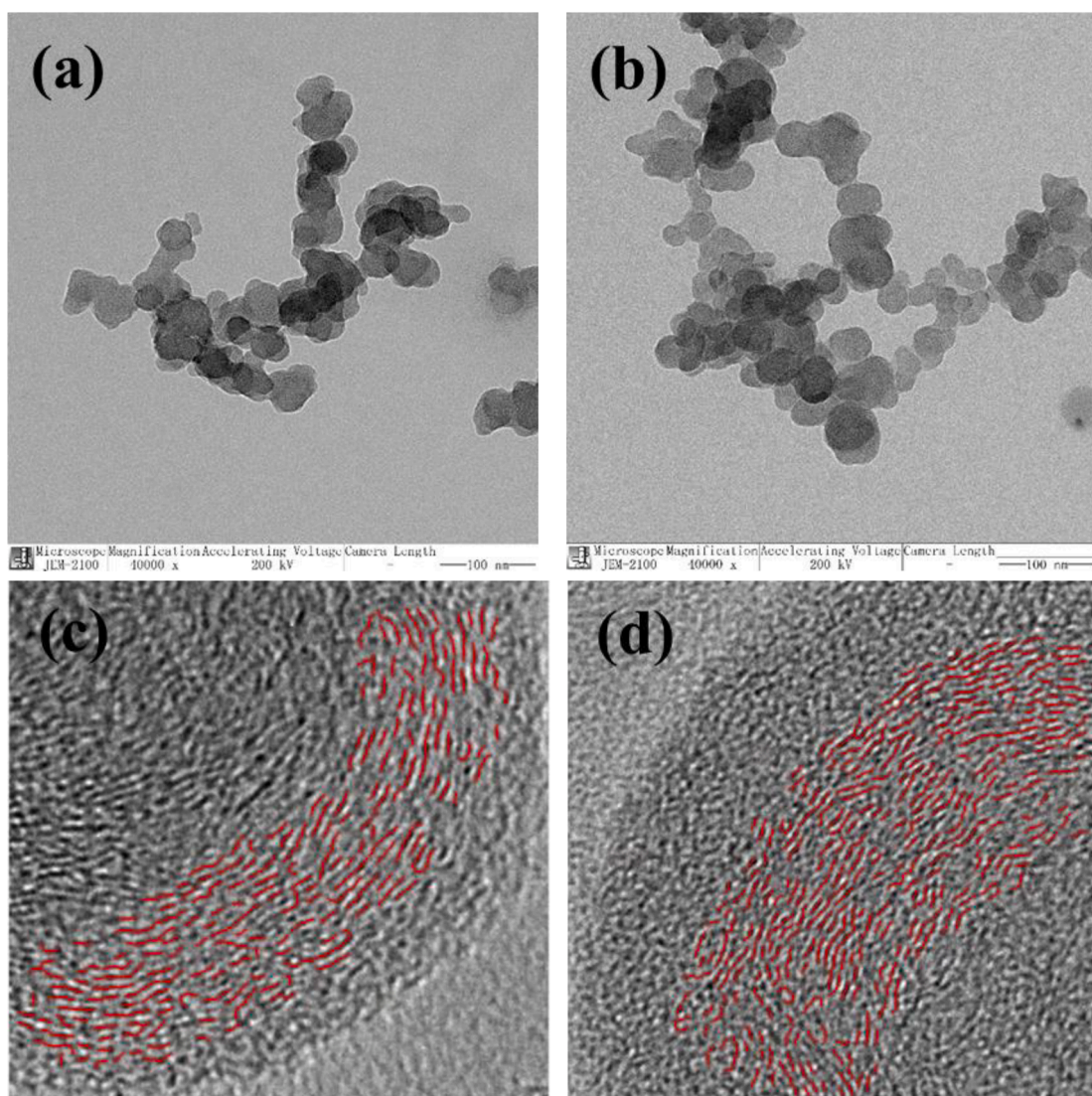


Fig. 7. TEM images of soot (a) Pye; (b) Pye-Na. And skeletons of soot samples (c) Pye; (d) Pye-Na.

The average number of lamellae  $n$  of Pye-Na pyrolytic soot is larger than that of Pye pyrolytic soot, and the addition of Na is beneficial to the stacking of the soot microchip layer structure. The trend of  $L_a$  is similar to that of  $n$ , indicating that the layer structure of the carbon microwafers

grows not only longitudinally (the number of layers  $n$  and the thickness of the microcrystalline structure increase [82]) but also laterally (the size of  $L_a$  within the face of the layer structure increases) during the growth of soot. This result was also confirmed in the Raman analysis.

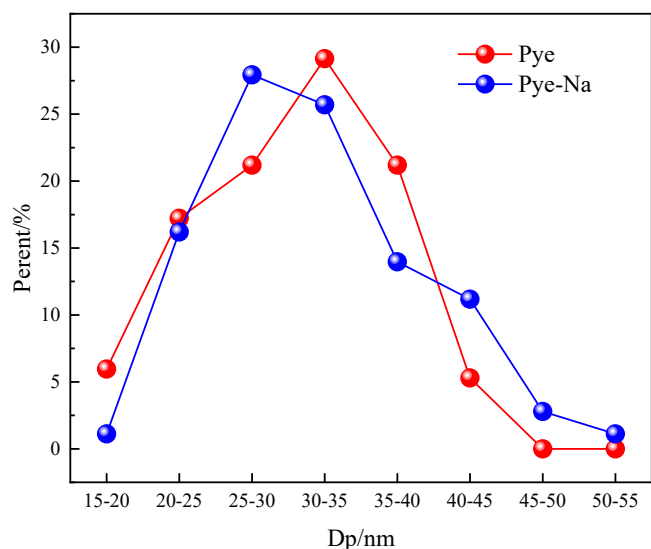


Fig. 8. The average particle size of basic soot particles produced by Pye and Pye-Na.

### 3.2.3. Chemical structure of the soot clusters

Fig. 12 (a) shows the FTIR spectra of soot. The figure illustrated that  $\text{NaNO}_3$  has greatly affected the peak region of the aromatic hydrogen ( $760\text{--}900\text{ cm}^{-1}$ ) and the  $\text{C}=\text{C}$  stretching vibration region of the aromatic ring ( $1492\text{--}1613\text{ cm}^{-1}$ ). The recorded FTIR spectra were processed with baseline correction and analyzed using deconvolution for further analysis.

The following parameters are used to characterize the changes in the aliphatic structure:  $I_a = A_{\text{aliphatic H}}/A_{\text{all}}$  and  $R_a = A_{\text{CH}_2}/A_{\text{CH}_3}$ . The parameters that characterize the change in aromatic structure are  $I_b = A_{\text{aromatic C=C}}/A_{\text{all}}$  and  $R_b = A_{\text{aromatic C-H}}/A_{\text{aromatic C=C}}$ . The parameters that characterize the changes in oxygen-containing functional groups are  $I_c = A_{\text{C-O}}/A_{\text{all}}$  and  $I_d = A_{\text{C=O}}/A_{\text{all}}$  [83].

Table 6 displays the changing trend of the chemical structure in soot before and after Na addition. The table shows that  $I_a$ ,  $R_a$ ,  $I_b$ , and  $R_b$  are significantly reduced after the addition of  $\text{NaNO}_3$ . The aliphatic content of soot decreases, the main chain of the aliphatic chain becomes shorter, and the branched-chain increases. Moreover, the content of the six-membered ring and aromatic substances in soot is reduced, Na and oxygenated substances react with aromatic substances to form sodium carboxylate and sodium phenol attached to the aromatic substances.

During the oxidation of soot, the aromatic compounds first react with hydroxyl groups to produce  $\text{C-O}$ , which is later oxidized to  $\text{C=O}$ . Then,  $\text{C=O}$  is separated from the aromatic ring to produce  $\text{CO}$  and later reacts with  $\text{O}$  in the environment to produce  $\text{CO}_2$  discharge. Therefore,  $I_c$  and  $I_d$  are reduced after the addition of Na.

The region of wavelength  $700\text{--}925\text{ cm}^{-1}$  is the aromatic hydrogen spectral band region, which is caused by the out-of-plane bending vibrations of the  $\text{C-H}$  bonds in the aromatic rings. As shown in Fig. 13. The  $875\text{ cm}^{-1}$  interval is associated with a single H (SOLO) bending vibration; bands round  $836$  and  $817\text{ cm}^{-1}$  are associated with two adjacent H (DUO) bending vibrations, and those near  $790$ ,  $755$ , and  $740\text{ cm}^{-1}$  are associated with three and four adjacent H (TRIO and QUATRO) bending vibrations [84,85]. Accordingly, the defects in the microcrystalline

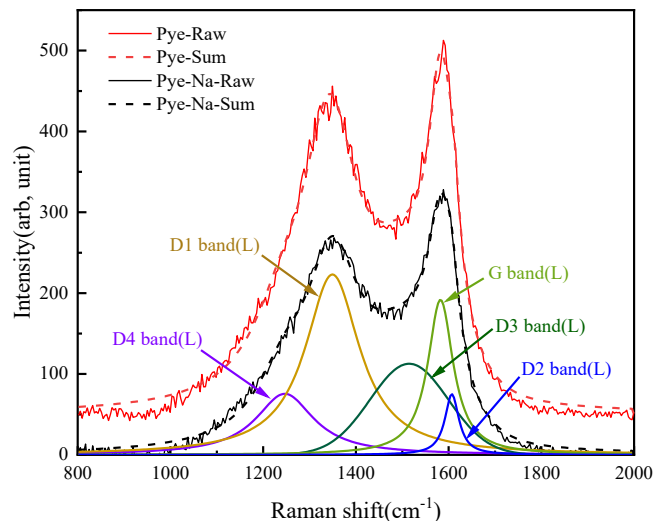


Fig. 10. First-order Raman spectra ( $800\text{--}2000\text{ cm}^{-1}$ ) of soot generated by Pye and Pye-Na.

Table 4

Comparisons between different Raman spectral parameters of soot particles emitted from Pye and Pye-Na.

	$R_2 = I_{D1}/(I_{D1} + I_G + I_{D2})$	$L_a = 4.35/(I_{D1}/I_G)$	$I_{D3}/I_G$	$FWHM_G$
Pye	0.70	1.54	1.04	30.84
Pye-Na	0.67	1.74	1.19	33.25

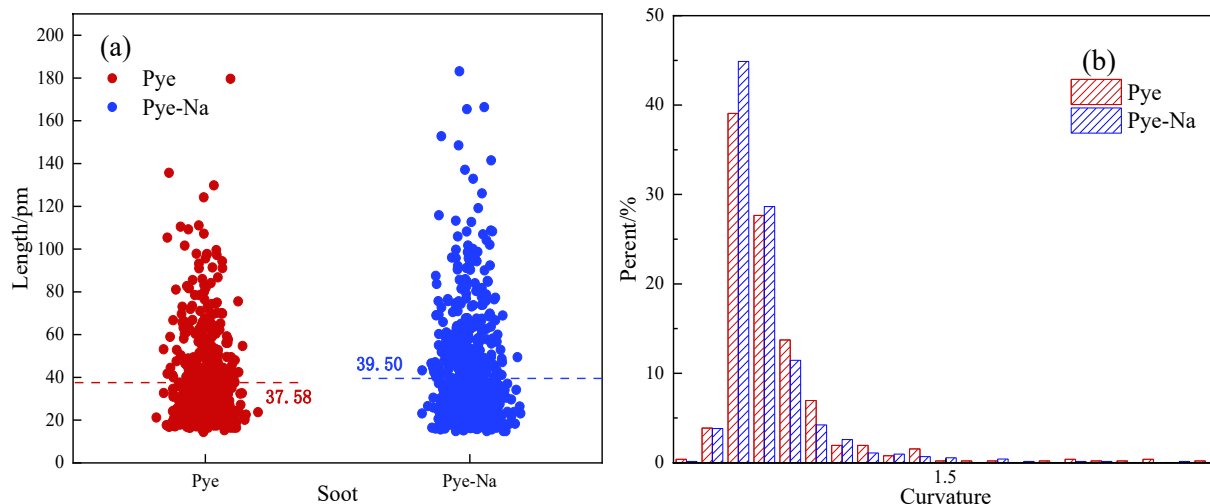


Fig. 9. Microcrystalline Characteristics of Soot Particles Produced by Pye and Pye-Na Pyrolysis (a)Length; (b)Curvature.

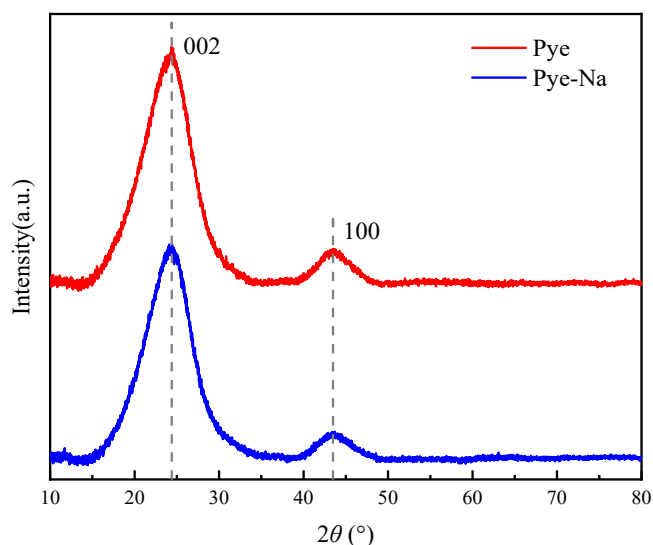


Fig. 11. XRD spectra of the soot derived from Pye and Pye-Na.

Table 5  
Characterizations of the graphitic microcrystalline.

	$d_{002}$	$L_{c(002)}$	$n$	$L_{a(100)}$
Pye	0.37	1.24	3.35	3.74
Pye-Na	0.37	1.25	3.40	3.90

carbon structure and the holes within the lamellae were analyzed by fitting this band. The ratio of SOLO within the lamellae with holes is higher than that of DUO. Meanwhile, the ratio of TRIO and QUATRO decreases with the increase in the basic structural units (BSU). Table 7 shows that SOLO/DUO increases from 2.01 to 2.54, and (TRIO + QUATRO)/All decreases from 0.41 to 0.38 after Na addition. Therefore, the lamellae of soot produced after Na addition increases, but the pores also increase, which is consistent with the XRD analysis.

The XPS peak splitting fits for Pye soot and Pye-Na soot are divided into six and three peaks for C1s and O1s energy regions, respectively, as shown in Fig. 14. The C peaks are divided into C=O ( $287.1 \pm 0.1$  eV), C–O ( $286.2 \pm 0.1$  eV),  $sp^2$  hybridized carbon ( $284.76 \pm 0.1$  eV),  $sp^3$  hybridized carbon ( $285.6 \pm 0.1$  eV), COO ( $289.2 \pm 0.1$  eV), and C–C full ( $283.6 \pm 0.1$ ). The O peaks are divided into C=O ( $532.1 \pm 0.2$  eV), R–O–R' ( $532.9 \pm 0.1$  eV), and R–OH ( $533.8 \pm 0.1$  eV) [86].

Fig. 15 displays the concentration of the chemical states present in

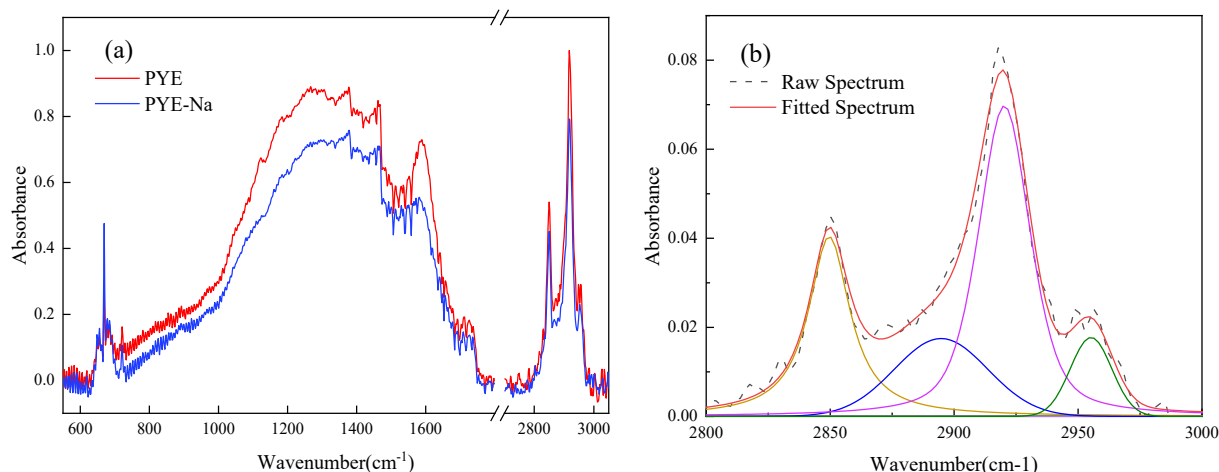


Fig. 12. Deconvolution of the FT-IR spectrum of Pye in the range of (a) 600–3000  $cm^{-1}$ , (b) 2800–3000  $cm^{-1}$ .

the C1s and O1s spectra. In the aforementioned figure, the  $sp^3$  hybridized carbon content, which is defined as defective carbon, significantly increased from 10.17% to 17.56% after the addition of Na, which is an increase of 74.34%. The  $sp^2$  hybridized carbon, which decreased from 62.32% to 61.23%, is considered nearly defect-free graphite. The O1s spectra of the two soot samples showed a significant decrease in the contents of the C=O and R–OH groups after the addition of Na. The

Table 6  
Chemical functional group parameters of Pye-soot and Pye-Na-soot.

	$I_a$	$R_a$	$I_b$	$R_b$	$I_c$	$I_d$
Pye	0.0970	6.099	0.0451	1.3485	0.2168	0.0333
Pye-Na	0.0730	4.1160	0.0370	0.9463	0.2021	0.0233

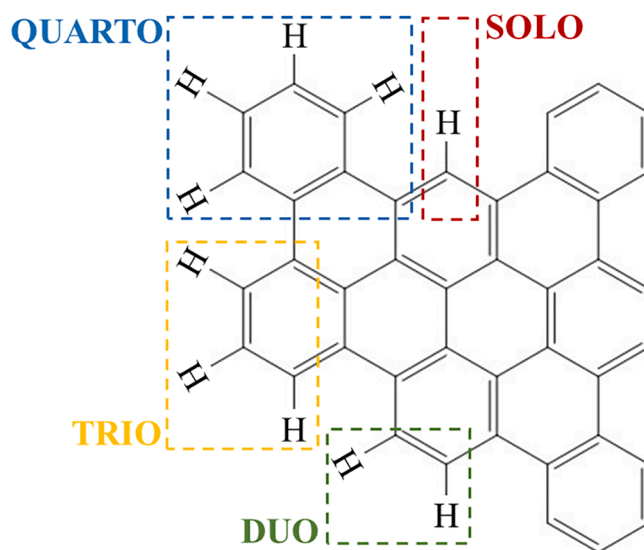


Fig. 13. The “defect borders” (solo, duo, trio and quatro adjacent hydrogens) of the basic structure units.

Table 7  
Area of the 700–925  $cm^{-1}$  peaks and variations of the peak area ratio.

	SOLO	DUO	TRIO	QUATRO
Pye	0.39	0.20	0.14	0.27
Pye-Na	0.44	0.17	0.13	0.25

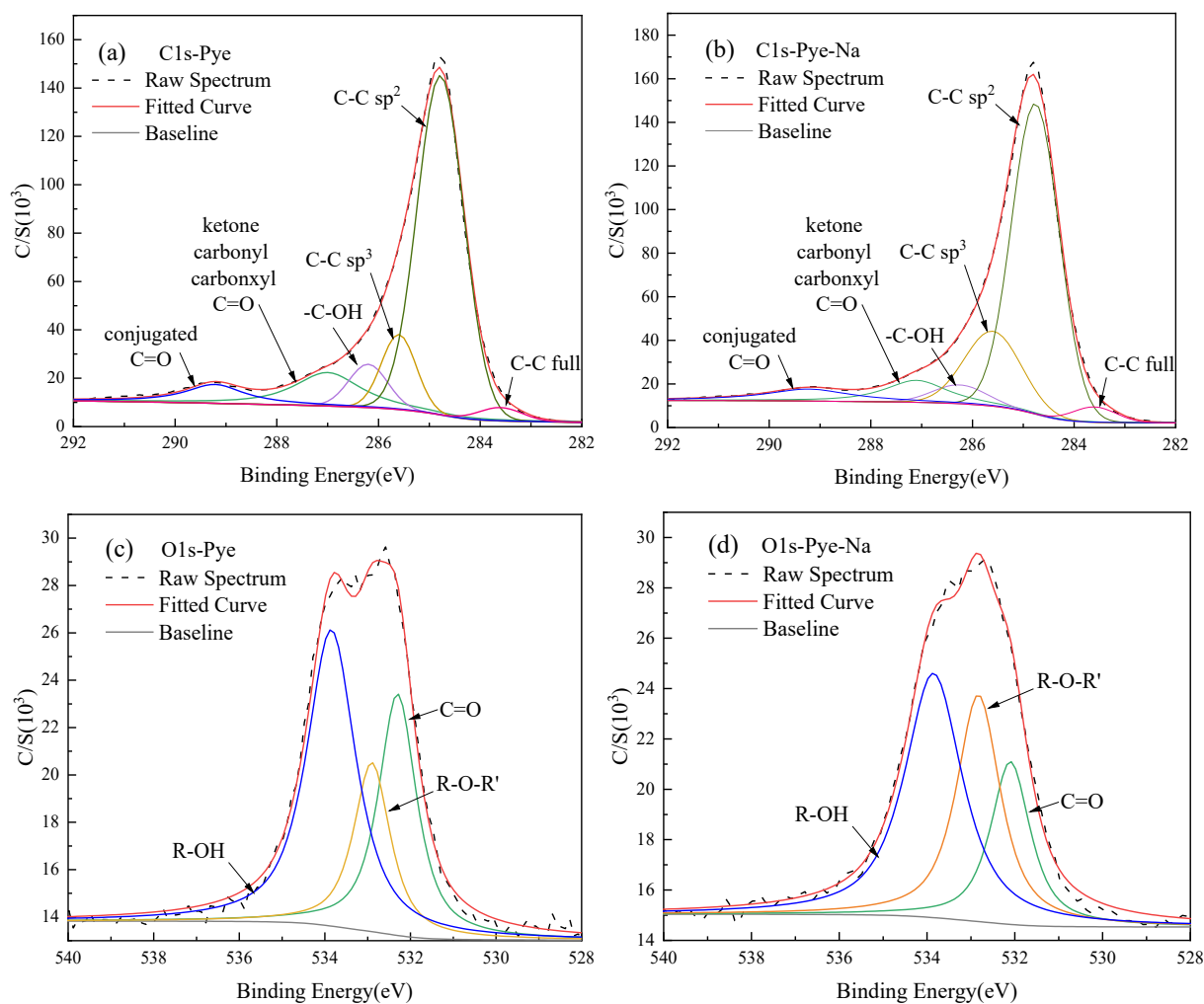


Fig. 14. XPS spectra and fitting results (a)Pye-C1s (b) Pye-Na-C1s (c) Pye-O1s (d) Pye-Na-O1s.

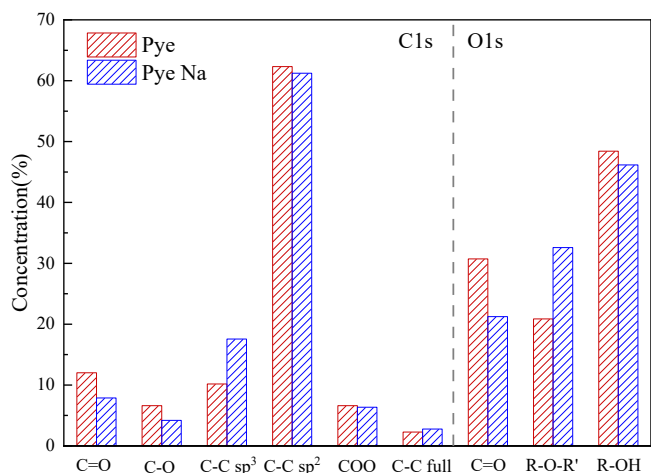


Fig. 15. Area proportion of Carbon/Oxygen in different chemical states on soot surface calculated from fitting result of XPS C1s/O1s spectrum.

addition of Na accelerates the oxidation of R-OH groups in soot to C=O, which is then further oxidized to CO and CO<sub>2</sub> as gas. The surface oxygen content of soot decreases, and the content of R-O-R' group increases, which is confirmed by Gaussian simulation and FTIR analysis.

This study used polycyclic aromatic hydrocarbon pyrene as the

reactant. A combination of DFT simulation and high-temperature sinker furnace pyrolysis experiments was carried out to compare the changes in energy, soot elements, microstructure, and chemical structure of the •OH oxidized pyrene radicals before and after the addition of Na. We provide reference and support for the reduction of particulate pollutant emissions and the development of functional carbon materials by analyzing the effect of alkali metal Na on the formation process of soot.

In this study, we followed the oxidation principle of Frenklach [33] and Edwards [32]. The effect of stable valence Na in the oxidation of pyrene radicals was simulated on the basis of electron transfer mechanism. Na acts as an “electron donor” to make the carbon atom more easily oxidized by changing the  $\pi$ -electron distribution of the benzene ring, thereby reducing the energy required for hydrogen transfer and facilitating the formation of a five-membered ring and releasing CO.

Na is easily gasified during coal pyrolysis and has a strong reactivity [28,30,76]. In this study, soot collected from the bottom of the sinker chamber was analyzed. The elemental analysis demonstrated that Pye-Na soot had decreased C/H and C/O compared with Pye soot. The microstructural analysis revealed that the peak particle size of Pye-Na soot decreased, the external microchip layer was oxidatively broken, the length and curvature of the internal microchip layer became larger, and the amorphous carbon content increased. The chemical structural analysis demonstrated that the aliphatic content of Pye-Na soot decreased, the Na-catalyzed oxidation of •OH in the surface microchip layer generated CO release, and the microchip layer gradually oxidized and flaked off. The internal microchip layer defects and pores increase,

and the soot histology decreases. The conclusions drawn from the experiments and simulations are in good agreement, both exhibit catalytic oxidation of sodium on PAHs and promote internal pore defects. The presence of defective structures within the carbon material is critical for directing the adsorption and catalytic behavior, and the pore structure enhances the adsorption storage capacity of the target species [31,87,88]. Therefore, the introduction of Na in the formation of coal-based soot is of great importance in terms of reducing pollutant emissions and in resource utilization.

#### 4. Conclusions

In this work, we analyzed the effect of alkali metal Na on the mechanism of PAHs-pyrene pyrolytically derived soot from the quantum chemical simulations and experiments. The oxidation pathways of the pyrene radicals before and after the addition of Na were constructed, and the characteristics of the soot (elemental component, chemical structure, and microstructure) were analyzed. This study provided new insights into the mechanism of PAH oxidation through the analysis of experimental studies and theoretical calculations. The specific results are as follows:

- (1) In the oxidation of pyrene radical by  $\cdot\text{OH}$ , the H transfer energy barrier on  $\cdot\text{OH}$  is the highest, which is the reaction speed control step.  $\text{Na}^+-\pi$  will change the charge distribution of pyrene radicals, lower the reaction energy barrier of the quick-control step, catalyze the reaction of pyrene radicals with  $\cdot\text{OH}$ , promote the formation of five-membered rings, and increase the curvature of the microchip layer because  $\text{Na}^+$  can attract O and promote H-transfer.
- (2) Na promoted the conversion of C–O functional groups to CO in soot, reduced the content of oxygen-containing functional groups, and caused the microchip layer on the surface of soot particles to be gradually oxidized and broken. The peak size of soot particles was reduced from 30–35 nm to 25–30 nm.
- (3) The addition of Na increased the C/H and C/O atomic ratios. The accelerated dehydrogenation condensation process in the presence of Na promoted the polymerization of small aromatic rings into highly polymerized aromatic structures, which increased the average length of the microchip from 1.54 nm to 1.74 nm. The detailed analysis of the structures of SOLO, DUO, TRIO, and QUARTO also revealed that Na could increase the BSU defects in the internal flakes of soot.
- (4) In this study, the theoretical calculations and experimental analyses demonstrated the promoting effect of alkali metal Na on the formation of internal pentacyclic rings in soot. The presence of Na resulted in longer microchip layers, increased curvature, better coating effect, and denser particle morphology. The results of the study can provide a theoretical basis for the directional regulation of soot structure.

#### CRedit authorship contribution statement

**Ziqi Zhao:** Methodology, Formal analysis, Investigation, Data curation, Data curation, Writing – original draft, Writing – review & editing. **Qian Du:** Conceptualization, Validation, Supervision. **Dun Li:** Methodology, Investigation. **Heming Dong:** Project administration. **Jianmin Gao:** Conceptualization, Validation. **Haibo Li:** Writing – review & editing. **Yu Zhang:** Writing – review & editing.

#### Declaration of Competing Interest

The authors declare that they have no known competing financial interests or personal relationships that could have appeared to influence the work reported in this paper.

#### Acknowledgments

The authors gratefully acknowledge financial support from the National Key Research and Development Project of China (2018YFF0216005).

#### References

- [1] Pérez S, Del Molino E, Barrio VL. Modeling and testing of a milli-structured reactor for carbon dioxide methanation. *Int J Chem Reactor Eng* 2019;17(11).
- [2] Zhang Y, Fang Y, Jin B, Zhang Y, Zhou C, Sher F. Effect of slot wall jet on combustion process in a 660 MW opposed wall fired pulverized coal boiler. *Int J Chem Reactor Eng* 2019;17(4).
- [3] Zulqarnain, Ayoub M, Yusoff MHM, Nazir MH, Zahid I, Ameen M, et al. A comprehensive review on oil extraction and biodiesel production technologies. *Sustainability* 2021;13(2):788.
- [4] Yaqoob H, Teoh YH, Sher F, Jamil MA, Nuhanović M, Razmkhah O, et al. Tribological behaviour and lubricating mechanism of tire pyrolysis oil. *Coatings* 2021;11(4):386.
- [5] Al-Juboori O, Sher F, Hazafa A, Khan MK, Chen GZ. The effect of variable operating parameters for hydrocarbon fuel formation from CO<sub>2</sub> by molten salts electrolysis. *Journal of CO<sub>2</sub> Utilization* 2020;40:101193.
- [6] Al-Juboori O, Sher F, Khalid U, Niazi MBK, Chen GZ. Electrochemical production of sustainable hydrocarbon fuels from CO<sub>2</sub> Co-electrolysis in eutectic molten melts. *ACS Sustainable Chem Eng* 2020;8(34):12877–90.
- [7] Sher F, Al-Shara NK, Iqbal SZ, Jahan Z, Chen GZ. Enhancing hydrogen production from steam electrolysis in molten hydroxides via selection of non-precious metal electrodes. *Int J Hydrogen Energy* 2020;45(53):28260–71.
- [8] Al-Shara NK, Sher F, Iqbal SZ, Curnick O, Chen GZ. Design and optimization of electrochemical cell potential for hydrogen gas production. *J Energy Chem* 2021;52:421–7.
- [9] Teh JS, Teoh YH, How HG, Sher F. Thermal analysis technologies for biomass feedstocks. A State-of-the-Art Review. *Processes* 2021;9(9):1610.
- [10] Cai S, Zhang S, Wei Y, Sher F, Wen L, Xu J, et al. A novel method for removing organic sulfur from high-sulfur coal: Migration of organic sulfur during microwave treatment with NaOH-H<sub>2</sub>O<sub>2</sub>. *Fuel* 2021;289:119800.
- [11] Disdier B, Arfi C, Pastor J, Pauli AM, Portugal H. Analysis by GC-MS of polycyclic aromatic hydrocarbons in a cream containing coal tar. *Polycyclic Aromat Compd* 2000;20(1–4):169–77.
- [12] Piacentini RD, Micheletti MI. Connections between black carbon (soot) emission and global warming. *Drying Technol* 2016;34(9):1009–10.
- [13] Jia H, Li S, Wu L, Li S, Sharma VK, Yan B. Cytotoxic free radicals on air-borne soot particles generated by burning wood or low-maturity coals. *Environ Sci Technol* 2020;54(9):5608–18.
- [14] Lin Y, Huang X, Liu Y, Cao D, Lu D, Feng Z, et al. Identification, quantification, and imaging of the biodistribution of soot particles by mass spectral fingerprinting. *Anal Chem* 2021;93(17):6665–72.
- [15] Ortega N, Curto A, Dimitrova A, Nunes J, Rasella D, Sacoer C, et al. Health and environmental impacts of replacing kerosene-based lighting with renewable electricity in East Africa. *Energy Sustain Dev* 2021;63:16–23.
- [16] Niranjan R, Thakur AK. The toxicological mechanisms of environmental soot (black carbon) and carbon black: focus on oxidative stress and inflammatory pathways. *Front Immunol* 2017;8:763.
- [17] Jawad AH, Mehdi ZS, Ishak M, Ismail K. Large surface area activated carbon from low-rank coal via microwave-assisted KOH activation for methylene blue adsorption. *Desalin Water Treatm* 2018;110.
- [18] Figueiredo JL, Pereira MFR. The role of surface chemistry in catalysis with carbons. *Catal Today* 2010;150(1–2):2–7.
- [19] Clague ADH, Donnet J, Wang TK, Peng JCM. A comparison of diesel engine soot with carbon black. *Carbon* 1999;37(10):1553–65.
- [20] Medalia AI, Rivin D, Sanders DR. A comparison of carbon black with soot. *Sci Total Environ* 1983;31(1):1–22.
- [21] Watson AY, Valberg PA. Carbon black and soot: two different substances. *AIHAJ* 2001;62(2):218–28.
- [22] Kanakaraj R, Sudakar C. Candle soot carbon nanoparticles as high-performance universal anode for M-ion (M = Li<sup>+</sup>, Na<sup>+</sup> and K<sup>+</sup>) batteries. *J Power Sources* 2020;458:228064.
- [23] Mulay MR, Chauhan A, Patel S, Balakrishnan V, Halder A, Vaish R. Candle soot: Journey from a pollutant to a functional material. *Carbon* 2019;144:684–712.
- [24] Yin C, Qiu S, Zhang S, Sher F, Zhang H, Xu J, et al. Strength degradation mechanism of iron coke prepared by mixed coal and Fe<sub>2</sub>O<sub>3</sub>. *J Anal Appl Pyrol* 2020;150: 104897.
- [25] Mannazhi M, Bergqvist S, Bengtsson P-E. Influence of potassium chloride on PAH concentration during soot formation studied using laser-induced fluorescence. *Combust Flame* 2022;235:111709.
- [26] Simonsson J, Olofsson N-E, Hosseinnia A, Bengtsson P-E. Influence of potassium chloride and other metal salts on soot formation studied using imaging LII and ELS, and TEM techniques. *Combust Flame* 2018;190:188–200.
- [27] Dong H, Zhang Yu, Du Q, Li D, Feng D, Gao J, et al. Roles of ion-exchangeable sodium in the conversion process of tar to soot during rapid pyrolysis of two brown coals in a drop-tube reactor. *ACS Omega* 2020;5(16):9078–92.
- [28] Ma P, Huang Q, Gao Qi, Li S. Effects of Na and Fe on the formation of coal-derived soot in a two-stage flat-flame burner. *Fuel* 2020;265:116914.

- [29] Xiao Z, Shang T, Zhuo J, Yao Q. Study on the mechanisms of ultrafine particle formation during high-sodium coal combustion in a flat-flame burner. *Fuel* 2016; 181:1257–64.
- [30] Dong H, Du Q, Li D, Feng D, Gao J, Wu S. Impact of sodium on the formation mechanism and physicochemical properties of coal-derived soot. *Energy Fuels* 2020;34(2):1453–66.
- [31] Li Y, Hu Y-S, Qi X, Rong X, Li H, Huang X, et al. Advanced sodium-ion batteries using superior low cost pyrolyzed anthracite anode: towards practical applications. *Energy Storage Mater* 2016;5:191–7.
- [32] Edwards DE, Zubarev DY, Lester Jr WA, Frenklach M. Pathways to soot oxidation: reaction of OH with phenanthrene radicals. *J Phys Chem A* 2014;118(37):8606–13.
- [33] Frenklach M, Liu Z, Singh RI, Galimova GR, Azyazov VN, Mebel AM. Detailed, sterically-resolved modeling of soot oxidation: Role of O atoms, interplay with particle nanostructure, and emergence of inner particle burning. *Combust Flame* 2018;188:284–306.
- [34] Zhao Z, Gao J, Du Q, Li D, Dong H, Zhang Yu, et al. Effect of Na on the condensation reaction of naphthalene molecules during coal pyrolysis. *J Energy Inst* 2021;98:313–21.
- [35] Han W, Liu G, Seo W, Lee H, Chu H, Yang W. Nitrogen-doped chain-like carbon nanospheres with tunable interlayer distance for superior pseudocapacitance-dominated zinc- and potassium-ion storage. *Carbon* 2021;184:534–43.
- [36] Azhar O, Jahan Z, Sher F, Niazi MBK, Kakar SJ, Shahid M. Cellulose acetate-polyvinyl alcohol blend hemodialysis membranes integrated with dialysis performance and high biocompatibility. *Mater Sci Eng C Mater Biol Appl* 2021; 126:112127.
- [37] Castoldi L, Matarrese R, Brambilla L, Serafini A, Tommasini M, Lietti L. Effect of potassium on a model soot combustion: Raman and HRTEM evidences. *Aerosol Sci Technol* 2016;50(4):405–15.
- [38] Soriano JA, Agudelo JR, López A, Armas O. Oxidation reactivity and nanostructural characterization of the soot coming from farnesane - A novel diesel fuel derived from sugar cane. *Carbon* 2017;125:516–29.
- [39] Chang Q, Gao R, Li H, Yu G, Wang F. Effect of CO<sub>2</sub> on the characteristics of soot derived from coal rapid pyrolysis. *Combust Flame* 2018;197:328–39.
- [40] Teixeira RA, Lima EC, Benetti AD, Thue PS, Cunha MR, Cimirro NFGM, et al. Preparation of hybrids of wood sawdust with 3-aminopropyl-triethoxysilane. Application as an adsorbent to remove Reactive Blue 4 dye from wastewater effluents. *J Taiwan Inst Chem Eng* 2021;125:141–52.
- [41] Lu T, Chen F. Multiwfn: a multifunctional wavefunction analyzer. *J Comput Chem* 2012;33(5):580–92.
- [42] Luo S, Zhao Y, Truhlar DG. Validation of electronic structure methods for isomerization reactions of large organic molecules. *Phys Chem Chem Phys* 2011;13(30):13683–9.
- [43] Li X, Xu X, You X, Truhlar DG. Benchmark calculations for bond dissociation enthalpies of unsaturated methyl esters and the bond dissociation enthalpies of methyl linolenate. *J Phys Chem A* 2016;120(23):4025–36.
- [44] Lu T, Chen Q. Interaction region indicator: A simple real space function clearly revealing both chemical bonds and weak interactions. *Chemistry* 2021;5.
- [45] Lu T, Chen F. Bond order analysis based on the Laplacian of electron density in fuzzy overlap space. *J Phys Chem A* 2013;117(14):3100–8.
- [46] Johnson ER, Keinan S, Mori-Sanchez P, Contreras-Garcia J, Cohen AJ, Yang W. Revealing noncovalent interactions. *J Am Chem Soc* 2010;132(18):6498–506.
- [47] Illinois Uo. **Visual molecular dynamics**. 2014.
- [48] Jing H, Zhun H, Jun Z, Shijin S. Effects of a catalyst on the nanostructure and reactivity of soot under an oxygen atmosphere. *Energy Fuels* 2016;30(3):2434–42.
- [49] Pascasio L, Martin JW, Menon A, Hou D, You X, Kraft M. Aromatic penta-linked hydrocarbons in soot nanoparticle formation. *Proc Combust Inst* 2021;38(1): 1525–32.
- [50] Singh R, Frenklach M. A mechanistic study of the influence of graphene curvature on the rate of high-temperature oxidation by molecular oxygen. *Carbon* 2016;101: 203–12.
- [51] van Setten BAAL, Makkee M, Moulijn JA. Science and technology of catalytic diesel particulate filters. *Catal Rev* 2001;43(4):489–564.
- [52] Yuan Q, Xu Z, Yakobson BI, Ding F. Efficient defect healing in catalytic carbon nanotube growth. *Phys Rev Lett* 2012;108(24):245505.
- [53] Su DS, Perathoner S, Centi G. Nanocarbons for the development of advanced catalysts. *Chem Rev* 2013;113(8):5782–816.
- [54] Chen J, Niksa S. The effects of secondary reactions on nitrogen distributions from rapid coal pyrolysis. *Coal Sci Proc* 1991:580–3.
- [55] Chen JC-Y. **Effects of secondary reactions on product distribution and nitrogen evolution from rapid coal pyrolysis**. Stanford University; 1991.
- [56] Richter H, Howard JB. Formation of polycyclic aromatic hydrocarbons and their growth to soot - a review of chemical reaction pathways. *Prog Energy Combust Sci* 2000;26(4–6):565–608.
- [57] Centrone A, Brambilla L, Renouard T, Gherghel L, Mathis C, Müllen K, et al. Structure of new carbonaceous materials: The role of vibrational spectroscopy. *Carbon* 2005;43(8):1593–609.
- [58] Zhang S, Lu J, Liu C, Feng Q. Characterization of micro-crystalline structure and particle size distribution of soot generated from MILD-OCC flame. *Fuel* 2020;267: 117259.
- [59] Raman CV, Krishnan KS. Polarisation of Scattered Light-quanta. *Nature* 1928;122 (3066).
- [60] Efremov EV, Ariese F, Gooijer C. Achievements in resonance Raman spectroscopy: Review of a technique with a distinct analytical chemistry potential. *Anal Chim Acta* 2008;606(2):119–34.
- [61] Das RS, Agrawal Y. Raman spectroscopy: recent advancements, techniques and applications. *Vib Spectrosc* 2011;57(2):163–76.
- [62] Feng D, Zhao Y, Zhang Yu, Xu H, Zhang L, Sun S. Catalytic mechanism of ion-exchanging alkali and alkaline earth metallic species on biochar reactivity during CO<sub>2</sub>/H<sub>2</sub>O gasification. *Fuel* 2018;212:523–32.
- [63] Commodo M, Karataş AE, De Falco G, Minutolo P, D'Anna A, Gülder ÖL. On the effect of pressure on soot nanostructure: A Raman spectroscopy investigation. *Combust Flame* 2020;219:13–9.
- [64] Saffaripour M, Tay L-L, Thomson KA, Smallwood GJ, Brem BT, Durdina L, et al. Raman spectroscopy and TEM characterization of solid particulate matter emitted from soot generators and aircraft turbine engines. *Aerosol Sci Technol* 2017;51(4): 518–31.
- [65] Le KC, Lefumeux C, Pino T. Watching soot inception via online Raman spectroscopy. *Combust Flame* 2022;236:111817.
- [66] Chu C, Naseri A, Mitra T, Dadsetan M, Sediako A, Thomson MJ. The effect of elevated reactant temperatures on soot nanostructures in a coflow diffusion ethylene flame. *Proc Combust Inst* 2021;38(2):2525–32.
- [67] Furukawa Y, Sakamoto A, Ohta H, Tasumi M. Raman characterization of polarons, bipolarons and solitons in conducting polymers. *Synth Met* 1992;49(1):335–40.
- [68] Al-Jishi R, Elman BS, Dresselhaus G. Lattice-dynamical model for graphite. *Mrs Proc* 1982;20(2):127.
- [69] Yw A, Mp A, Hh A, Xz A, Jw B, Hao CC. Physicochemical properties of exhaust soot from lower and higher alcohols: Characterizations and impact on soot oxidation behavior. 2021.
- [70] Ess MN, Ferry D, Kireeva ED, Niessner R, Ouf FX, Ivleva NP. In situ Raman microspectroscopic analysis of soot samples with different organic carbon content: Structural changes during heating. *Carbon* 2016;105:572–85.
- [71] Le KC, Pino T, Pham VT, Henriksson J, Török S, Bengtsson P-E. Raman spectroscopy of mini-CAST soot with various fractions of organic compounds: Structural characterization during heating treatment from 25 °C to 1000 °C. *Combust Flame* 2019;209:291–302.
- [72] Zhang H, Li S, Jiao Y, Emil iojoiu E, Da Costa P, Elena Galvez M, et al. Structure, surface and reactivity of activated carbon: From model soot to Bio Diesel soot. *Fuel* 2019;257:116038.
- [73] Pawlyta M, Rouzaud JN, Duber S. Raman microspectroscopy characterization of carbon blacks: Spectral analysis and structural information. *Carbon* 2015;84: 479–90.
- [74] Tuinstra F, Koenig JL. Raman spectrum of graphite. *J Chem Phys* 1970;53(3): 1126–30.
- [75] Wu Y, Zhang Yu, Zhuo J, Yao Q. Effect of ion-exchangeable calcium on carbonaceous particulate matter formation during coal pyrolysis. *Fuel* 2022;315: 123124.
- [76] Zhang H, He J, Li S, Iojoiu EE, Galvez ME, Xiong H, et al. Effect of Biodiesel impurities (K, Na, P) on non-catalytic and catalytic activities of Diesel soot in model DPF regeneration conditions. *Fuel Process Technol* 2020;199:106293.
- [77] Ishiguro T, Takatori Y, Akihama K. Microstructure of diesel soot particles probed by electron microscopy: First observation of inner core and outer shell. *Combust Flame* 1997;108(1):231–4.
- [78] Ying Y, Liu D. Effects of water addition on soot properties in ethylene inverse diffusion flames. *Fuel* 2019;247:187–97.
- [79] Liu Y, Fan C, Wang X, Liu F, Chen H. Thermally induced variations in the nanostructure and reactivity of soot particles emitted from a diesel engine. *Chemosphere* 2022;286(Pt 2):131712.
- [80] Yehliu K, Vander Wal RL, Armas O, Boehman AL. Impact of fuel formulation on the nanostructure and reactivity of diesel soot. *Combust Flame* 2012;159(12): 3597–606.
- [81] Gogoi B, Raj A, Alrefaai MM, Stephen S, Anjana T, Pillai V, et al. Effects of 2,5-dimethylfuran addition to diesel on soot nanostructures and reactivity. *Fuel* 2015; 159:766–75.
- [82] Feng D, Shang Qi, Dong H, Zhang Yu, Wang Z, Li D, et al. Catalytic mechanism of Na on coal pyrolysis-derived carbon black formation: experiment and DFT simulation. *Fuel Process Technol* 2021;224:107011.
- [83] Chang Q, Gao R, Gao M, Yu G, Wang F. The structural evolution and fragmentation of coal-derived soot and carbon black during high-temperature air oxidation. *Combust Flame* 2020;216:111–25.
- [84] Russo C, Stanzione F, Tregrossi A, Ciajolo A. Infrared spectroscopy of some carbon-based materials relevant in combustion: Qualitative and quantitative analysis of hydrogen. *Carbon* 2014;74:127–38.
- [85] Dias JR. Edge effects in benzenoid and total resonant sextet benzenoid hydrocarbons and Clar's sextet principle. *J Phys Chem A* 2019;123(14):3229–38.
- [86] Cadrazco M, Santamaria A, Agudelo JR. Chemical and nanostructural characteristics of the particulate matter produced by renewable diesel fuel in an automotive diesel engine. *Combust Flame* 2019;203(5):130–42.
- [87] Wang L, Wang R, Zhao H, Liu L, Jia D. High rate performance porous carbon prepared from coal for supercapacitors. *Mater Lett* 2015;149:85–8.
- [88] Sun F, Gao J, Yang Y, Zhu Y, Wang L, Pi X, et al. One-step ammonia activation of Zhundong coal generating nitrogen-doped microporous carbon for gas adsorption and energy storage. *Carbon* 2016;109:747–54.